An X-ray powder diffraction study of damage produced in Ca(OH)2 and Mg(OH)2 by electron irradiation using the 2.5 MeV SIRIUS accelerator

Marie-Noëlle de Noirfontaine, Loren Acher, Mireille Courtial, Frederic Dunstetter, Dominique Gorse-Pomonti

An X-ray powder diffraction study of damage produced in $Ca(OH)_2$ and $Mg(OH)_2$ by electron irradiation using the 2.5 MeV SIRIUS accelerator

[1]Marie-Noëlle de Noirfontaine, [1,2]Loren Acher, [1,3]Mireille Courtial, [1]Frédéric Dunstetter, [1*]Dominique Gorse – Pomonti

[1]Laboratoire des Solides Irradiés, Ecole Polytechnique, CNRS UMR 7642, CEA-DSM-IRAMIS, Université Paris-Saclay, F-91128 Palaiseau Cedex, France
[2]Laboratoire d'études des Ciments et Bitumes pour le Conditionnement (LCBC) - CEA-DEN, DE2D/SEAD/LCBC - Marcoule, F-30207 Bagnols-sur-Cèze, France
[3]Université d'Artois, 1230 Rue de l'Université, F-62408 Béthune, France

*Corresponding author.
E-mail address: dominique.gorse-pomonti@polytechnique.edu (D. Gorse - Pomonti)
Tel.: +33 1 69 33 45 24; fax: +33 1 69 33 45 54

Abstract

Two isomorphous hydrous minerals, $Mg(OH)_2$ and $Ca(OH)_2$, were exposed to the 2.5 MeV electron beam of the SIRIUS accelerator platform. Both compounds remain stable under the beam up to high doses, in the range of 3 – 3.5 GGy. No decomposition is observed.

But contrary to earlier statements, a net difference of reactivity between them is highlighted as a result of the present X-ray powder diffraction study: i) a significant dilatation is observed along the *c* - axis, more significant in brucite than in portlandite as already reported during thermal decomposition studies, ii) but a contraction is here revealed in the basal plane of brucite, along the *a* – axis, while a slight dilatation is still being observed in portlandite. Contraction in the basal plane seems a specific feature of electron irradiation only once previously observed by TEM in brucite. Moreover for brucite, the decreasing intensities of Bragg lines together with the appearance of a diffuse scattering over the whole angular range is compatible with the appearance of some static structural disorder induced by electron irradiation. Finally electron irradiation leads to a significant reduction in crystallite size with increasing dose, by a factor of 2 at the intermediate dose of 310 MGy in brucite, while for a comparable effect to occur an absorbed dose of 3.5 GGy should be attained in portlandite.

1. Introduction

Brucite $Mg(OH)_2$ and portlandite $Ca(OH)_2$ are isomorphous [1, 2, 3]. They belong to the family of CdI_2 type hydroxides with a layered structure, giving them interesting physico-chemical and electronic properties for a large number of industrial applications. The M (M = Ca, Mg) cations are placed at the centre of edge-sharing $[MO_6]$ octahedra (Fig. 1): they are bonded to six neighboring

hydroxyl ions and the hydroxyl ions are bonded to three M cations. The space group is $P\bar{3}m1$ (n°164). The cell parameters are respectively a = 3.5918 Å and c = 4.9063 Å (c/a = 1.3659) in portlandite [2] and a = 3.1497 Å and c = 4.7702 Å (c/a = 1.5145) in brucite [3]. The cell parameters of the refined structure model proposed by Chaix-Pluchery et al. are used for portlandite [2], since their neutron diffraction study specifies accurately the H atoms positions and the O-H bond lengths. The octahedra are said flattened, compared to regular octahedra formed with close-packed spheres for which an higher c/a ratio of 1.633 is calculated [4]. The interlayer spacing h(inter), defined by Brindley et al. [4], decreases from h(inter) = 2.689 Å in brucite to h(inter) = 2.616 Å in portlandite, after Desgranges et al. [5]. The recently calculated electronic structure of brucite and portlandite reveals only slight differences between them [6].

The thermal decomposition of $Mg(OH)_2$ into MgO under the electron beam and of isotructural compounds like $Ca(OH)_2$, has been largely studied for over fifty years by neutron diffraction, X-ray diffraction and electron microscopy [2, 7 - 12]. It was finally concluded that the thermal and electron-beam-induced transformation are identical and that this transformation is pseudomorphic and topotactic in spite of a huge volume reduction between the initial and final phase, involving the proton mobility, formation of H_2O molecules from hydroxyl ions sites OH^- and elimination along the 00l cleavage planes followed by the "final" structural transformation. Note that the complete decomposition of $Mg(OH)_2$ into MgO at "high" flux under the 80 keV electron beam of a microscope has been reported as early as 1958 by Goodman [7] and was said to proceed in a highly ordered manner, topotactically, by simple rearrangement of the atoms of the parent crystal, already by Goodman [7] and later by Dahmen and coworkers [10].

The NEC Pelletron accelerator of the SIRIUS platform is used here to study the radiation damage effects caused by electron irradiation to portlandite $Ca(OH)_2$ and brucite $Mg(OH)_2$. Portlandite enters in the composition of the Portland cement pastes today proposed for the conditioning of nuclear wastes [13]. It is thus essential to determine its structural stability and resistance under (somehow) representative irradiation conditions, while brucite is being studied here for comparison purposes.

There is today a substantial literature on electron radiation damages in ceramics, including complex ceramics proposed for nuclear waste disposal, as a function of the irradiation conditions, especially energy, dose and temperature [14-16]. The dependency with respect to radiation flux was clearly far less studied for the obvious reason that two experimental techniques are necessary to cover a wide range of flux values, a Transmission Electron Microscope (TEM) for "high" electron fluxes (from ~10^{17} to a few 10^{22} $e^-.cm^{-2}.s^{-1}$) and a linear electron accelerator for "low" electron fluxes (in the range of 10^{13} to a few 10^{14} $e^-.cm^{-2}.s^{-1}$), with no overlap between them. The influence of electron irradiation at low flux on the structural properties of ceramics has been scarcely studied to date and it is often said that no significant electron radiation damage could be created at low electron flux and dose and that exposure to the intense electron beam of a TEM is required to seriously damage ceramic materials. We

shall see later that brucite and porlandite are sensitive to electron irradiation for a flux of order 10^{14} $e^-.cm^{-2}.s^{-1}$ and an absorbed dose of a few hundred MGy.

The slowing down of electrons through matter, as for other types of projectile and it is not different actually from other light or not projectiles (with exception of swift heavy ions), is caused by both electron excitations or ionizations of target atoms and subsequent radiolytic reactions (referred to as inelastic electronic energy loss) and ballistic collisions with target nuclei giving rise to atomic displacements (referred to as elastic nuclear energy loss) [17, 18]. When changing the projectile nature and velocity, only the balance between the two energy loss mechanisms will be affected. As for electron irradiation, two contradictory statements can be found in the literature. On the one hand, it is widely accepted that the contribution of ballistic collisions to an incident electron slowing down is negligible compared to that of the electronic excitations generated by its passage, and that over a wide energy range in excess of 1 MeV or above. But on the other hand if we go a little further, it appears that there are some radiation damages effects following electron irradiation which cannot be fully explained without taking into account some atomic displacements in the crystal lattice. This has been shown in rather recent studies dealing with ceramics foreseen for nuclear waste immobilization [19].

To the best of our knowledge, nothing is known about electron-radiation damage effects in $Ca(OH)_2$ and $Mg(OH)_2$, but only in CaO and MgO crystals. It was stated in 1984 by W. Hayes and A.M. Stoneham that radiolysis of oxides such as CaO and MgO does not result in production of vacancies and interstitials [20]. Since then this statement has apparently not been contradicted. It is also known that the threshold displacement energies, both cationic and anionic, are high in CaO and in MgO [21], which would not be in favour of a significant contribution of ballistic collisions to the electron radiation damage in both oxides and hydroxides. To be clear there is no indication in the literature about the possible cause of electron radiation damages in both brucite and portlandite. Coming back to the comparison between CaO and MgO, it is noteworthy that in 1966, Matzke and Whitton studied the ion–irradiation effects on a series of cubic single crystals (among them CaO and MgO) and non-cubic single crystals and in doing so that they have shown by electron diffraction that among the cubic crystals only MgO is damaged under 40 keV rare gas ion irradiation up to a dose of 2×10^{16} ion cm^{-2}, with lattice disorder observed without phase change (as mentioned by the authors) in MgO, in contrast with other cubic crystals, like CaO, that all remain undamaged [22].

In this paper, Powder X-ray Diffraction is used to analyze the irradiated hydroxides. Beyond identification of (perfect) crystalline phases and unit cell dimensions (peak positions and indexation), XRD is sensitive to deviations from perfect crystals taking the form of any structural disorder (whatever its origin, induced by irradiation, ball-milling …), provided that the defects are correlated at long distance and that the defective structure exhibits a long range correlated disorder [23]. Information on this point is contained in the shape of the diffraction spectra and the structured background between the diffraction peaks. However the point is that electron irradiation does not give rise to displacement cascades, but only to isolated point defects. So a priori one might wonder whether XRD is the suitable

tool to study electron radiation damages. Moreover we are also well aware of the fact that hydrogen is a weak scatterer and that the charge density distribution of hydrogen in both compounds is not directly accessible by XRD.

However, in this paper, and in spite of these non negligible drawbacks, significant changes in the XRD patterns of brucite and portlandite are observed following electron irradiation at low flux and doses in the range of 0.3 to 3 GGy. And a substantial difference in behavior under electron irradiation between the two compounds is highlighted.

2. Experimental

2.1 Materials

Commercial powders of portlandite $Ca(OH)_2$ (Prolabo, 96 wt.% purity) and of brucite $Mg(OH)_2$ (Prolabo, 99,7 wt. % purity) were used in this study. The impurity content was determined by X-ray fluorescence. For brucite, the impurities are: SiO_2: 0.845 wt.%, SO_3: 0.068 wt.%, CaO: 0.061 wt.%, Fe_2O_3: 0.008 wt.%, TiO_2: 0.002 wt.%, K_2O: 0.001 wt.%, P_2O_5: 0.001 wt.%. For porlandite, the main impurities are: MgO: 0.838 wt.%, SiO_2: 0.406 wt.%, Al_2O_3: 0.084 wt.%, Fe_2O_3: 0.071 wt.%, SO_3: 0.048 wt.%, MnO: 0.022 wt.%, Cl: 0.005 wt.%, TiO_2: 0.001 wt.%. In ambient air, some unavoidable carbonation of the portlandite powder occurs according to the reaction $Ca(OH)_2 + CO_2 \rightarrow CaCO_3 + H_2O$. Consequently the presence of a significant amount of calcite or/and vaterite will be found by XRD in the portlandite sample [24]. For irradiation experiments the powders are pressed in order to make discs of 13 mm diameter (1.33 cm^2) and about 1 mm thickness.

2.2 Electron irradiation conditions and energy loss in the target

The irradiation conditions are reported in Table 1. The accelerator NEC Pelletron of the SIRIUS platform (Ecole Polytechnique, Palaiseau, France) was used for electron irradiation at 2.5 MeV. At this energy all electrons pass through the sample, the projected range being in the order of 4 mm. The values of average beam current are 20 μA and 25 μA, the corresponding fluxes ϕ are equal to 9.5 x 10^{13} $e^-.cm^{-2}.s^{-1}$ and 1.2 x 10^{14} $e^-.cm^{-2}.s^{-1}$ respectively. The fluence Φ ranges from 7.4 x 10^{17} $e^-.cm^{-2}$ to 9.6 x 10^{18} $e^-.cm^{-2}$.

The energy loss in the target is then estimated. The total inelastic energy loss is calculated using the ESTAR code [25], based on the Bethe theory that gives an expression of the stopping power for fast electrons due to inelastic collisions events with electrons in a target of electron density NZ_2 (N atoms per unit volume of material of atomic number Z_2) [26]. The average energy loss per unit path length writes as:

$$-\left[\frac{dE}{dx}\right]_{inel} = \frac{2\pi e^4}{m_e v_1^2} NZ_2 \left\{\ln\left(\frac{m_e v_1^2 E_1}{2I^2(1-\beta^2)}\right) + F(\beta^2)\right\} \quad (1)$$

With: $F(\beta^2) = 1 - \beta^2 - \left(2\sqrt{1-\beta^2} - 1 + \beta^2\right)\ln 2 + \frac{1}{8}\left(1 - \sqrt{1-\beta^2}\right)^2$

where m_e, v_1 and E_1 refer respectively to the electron mass, velocity and total energy, and with $\beta = v_1/c$ (c = speed of light in vacuum) to take into account the relativistic character of the electrons.

Appearing in equation (1) as a logarithm, I refers to the mean excitation energy of the target [17]. A value of about 44 eV, almost the same for both portlandite and brucite, is used. This choice could be justified according to recent electronic structure calculations of both hydroxides [6], revealing only slight differences in electronic density distribution between $Mg(OH)_2$ and $Ca(OH)_2$. Consequently, the inelastic energy loss, and in fine the structural damages, should be comparable in the two materials. The total inelastic stopping power is reported in Table 2. The absorbed doses (in Gy) are then deduced: $\left[\frac{dE}{dx}\right]_{inel}$ **x** Φ/ρ, using 1Gy= 1J/kg (Table 1).

Energy loss via elastic collisions between electrons and target nuclei also contributes to the stopping power, giving rise to atomic displacements and possibly in fine well separated point defects. If sufficient energy is transferred to target nuclei, small cascades are possible. We have reported in Table 3 the maximum transferrable energy, T_{max} in eV, by electrons to the target atoms of atomic mass A during a head-on collision at 2.5 MeV, and 100, 200 keV for comparison, using:

$$T_{max} = E_1(E_1 + 2m_e c^2)/M_2 c^2 \quad (2)$$

or equivalently using $m_e c^2 = 511\, keV$, $T_{max} = 2147.7 \times E_1(E_1 + 1.022)/A$, with E_1 being the incident electron energy expressed in MeV.

The elastic scattering cross sections, or displacement cross sections σ_d, as a function of the electron projectile energy were then calculated up to 2.5 MeV for Mg, Ca and O atoms, using the SMOTT/ POLY code based on the model proposed by D. Lesueur [28]. This model takes into account elastic collisions with atoms of different atomic mass and number and possible displacement cascades (primary elastic collisions due to the incident electrons and also secondary elastic collisions due to recoil nuclei with all target elements), neglects the electronic slowing down, and also both long range and local order in the solid target considered as amorphous. As input data, the threshold displacement energies E_d are required. We used the E_d values measured for magnesium and oxygen in an MgO crystal (E_d(Mg) = 52 eV and E_d(O) = 54 eV [20, 21, 29]), and that measured for calcium and oxygen in a CaO crystal (E_d(Ca) = 50 eV and E_d(O) = 50 eV [20, 21, 29]), considering that the local octahedral environment is unchanged, or only slightly distorted from CaO to $Ca(OH)_2$, and from MgO to $Mg(OH)_2$. This is not an unreasonable assumption. The displacement cross sections of oxygen atoms in both brucite and portlandite are comparable above 1 MeV, this is less the case for the metal cations (Fig. 2). The displacement cross section of hydrogen is even not mentioned, which would be found very similar in the two compounds so long as the effective positive charge on the hydrogen atoms and effective negative charge on the OH^- anions [6] are not taken properly into account. The σ_d values should vary between about 20 and 50 barn for Ca and Mg atoms for 2.5 MeV electrons depending on the E_d values. The

maximum doses, expressed in dpa, estimated as the product $\sigma_d \Phi$, are reported in Table 1 for two values of displacement cross sections.

2.3 Powder X-ray diffraction

X-ray diffraction (XRD) data were collected using a powder X-ray diffractometer (X'Pert Pro Model, MPD, Panalytical) in the Bragg-Brentano geometry (θ/θ). The experimental configuration is as follows: the incident X-ray beam (Cu radiation, 45 kV, 40 mA) passes through a 0.5° divergence slit, a 0.02 rad Soller slit, a 1° anti-scatter slit, and a 10 mm beam mask before sample, and the diffracted beam through a 5.5 mm anti-scatter slit, a Ni Kβ filter, a 0.02 rad Soller slit before entering a fast X'Celerator detector of 2.546° (2θ) aperture. The instrument is operated in step-scan mode between 5° and 90° (2θ), with 0.02° (2θ) per step and 200 s step-time at room temperature.

Rietveld refinements are performed using TOPAS software (TOPAS, version 4.2, Bruker-AXS, Karlsruhe, Germany, 1999–2009) based on the fundamental parameters approach [30, 31]. The line profile of the Bragg peaks is represented as the convolution of the instrumental function, which is calculated as the convolution of the source function and all optical elements on the incident beam trajectory, and of an intrinsic diffraction profile representing the sample contribution with its specific microstructure.

For all adjustments, the refined parameters are the following: phase scale factor, zero-shift error, coefficients of the background described as a fifth order Chebychev polynomial combined with a 1/X term, unit cell parameters and crystallite size. The atomic positions and temperature factors are kept constant in the crystal structures. The structural data respectively reported by Chaix-Pluchery et al. [2] for $Ca(OH)_2$, by Catti et al. [3] for $Mg(OH)_2$, by Maslen et al. [31] for calcite and by Kahmi [32] for vaterite were used. Preferred orientation along the [001] axis is corrected using the March-Dollase algorithm [33].

Here, crystallite means a coherent scattering domain, which can be smaller than the grain size because of extended structural defects (grain boundaries or dislocations), resulting in a loss of coherency. Electron – irradiation may cause displacements of atoms from their ideal position, giving rise to lattice microstrains, and also change the crystallite size.

To go deeper inside the microstructural analysis and get some quantitative information, two analyses were performed, one assuming a monodispersed distribution of spherical (or quasi-spherical) crystallites (resulting in an isotropic line broadening) and a second one always assuming a monodispersed distribution of crystallites but taking into account a possible shape anisotropy (resulting in an anisotropic line broadening).

2.3.1 Integral-breath method

This first method is used for determining the volume – weighted crystallite size and lattice microstrain, which are varying in 2θ as a function of 1/cosθ and tanθ respectively [34]. The integral breadth β is given by the line profile area divided by the peak maximum intensity for each hkl reflection:

$$\beta = I_{max}^{-1} \int_{2\theta_0-\sigma}^{2\theta_0+\sigma} I(2\theta)\, d(2\theta) \tag{3}$$

where σ refers to the truncation of the Bragg peak profile at position of maximum intensity $2\theta_0$. It is used to define the peak width. Then, according to Scherrer, the apparent volume-averaged crystallite size ε_β in the direction normal to the reflecting plane (hkl) writes:

$$\varepsilon_\beta = \lambda / \beta \cos\theta \quad (\theta \text{ in radians}) \tag{4}$$

In fact ε_β is just the volume – averaged mean thickness of the crystallites measured perpendicularly to the reflecting planes [35, 36]. ε_β is also written as L_{Vol} or $LVOL-IB$, the so-called volume - weighted column height in TOPAS-4. Assuming a monodispersed system of spherical crystallites, after Wilson [35], we deduce the diameter of the sphere D (in nm) using:

$$\langle D \rangle_V = \tfrac{4}{3}\, \varepsilon_\beta \tag{5}$$

Now let ε_0 be the maximum lattice deformation (or strain). The interplanar spacing d will vary of $\pm\varepsilon_0$ ($\varepsilon_0 = \delta d/d$). Directly deduced from the Bragg law, the reflections will be appreciable over an angular range equal to $4\,\varepsilon_0 \tan\theta$, in 2θ. An upper limit of the lattice deformations in the crystallites is thus obtained, using:

$$\varepsilon_0 = \beta / (4 \times \tan\theta) \tag{6}$$

where β is the integral breadth defined above.

In TOPAS, the intrinsic diffraction profile is represented by a Voigt function, as a result of the convolution of two Voigt functions, one for the crystallite size and the other for lattice microdistortions [34]. Both crystallite size and strain parameters are refined, giving access to an apparent volume-averaged crystallite size L_{Vol} (in nm) and a mean microstrain value ε_0 (in %).

2.3.2 Variance method

This second method allows for determining an average surface-weighted crystallite size [35-37]. The projected surface of the crystallite volume in the direction [hkl] is directly calculated in real space. In case of anisotropic shape, there will be different apparent crystallite sizes $\varepsilon_{k(hkl)}$ for the corresponding Bragg peaks, defined as:

$$\varepsilon_{k(hkl)} = V / A_{(hkl)} \tag{7}$$

where V is the crystallite volume and $A_{(hkl)}$ its area projected on a plane parallel to the reflecting planes (hkl). There will be also different Scherrer constants $K_{k(hkl)}$ defined as:

$$K_{k(hkl)} = \sqrt[3]{V}/\varepsilon_{k(hkl)} = D_A/\varepsilon_{k(hkl)}, \text{ using } D_A = \sqrt[3]{V} \quad (8)$$

Now we use an expression of the surface-weighted crystal size proposed by Sanchez-Bajo [38], assuming a purely lorentzian line profile:

$$\langle D \rangle_A = \frac{180\,\lambda\,K_{K(hkl)}}{\pi^2 H_L \cos\theta} \quad (9)$$

where H_L is the Lorentzian full width at half maximum.

Based on the above formalism, the so-called "AnisoCS" routine, developed by Ectors *et al.* [39-40], was implemented into the TOPAS software. This approach has proven to be effective in the case of different geometric models of crystallite. Note that no lattice distortions are taken into account in this model, the line broadening being supposed entirely due to a crystallite size effect. In other words, the crystallites are supposed strain free.

In the present work, the crystallites are assumed cylindrical, with the flat cylindrical face normal to the [001] direction. The averaged dimensions of the cylinders D_{001} (height in nm) and D_{100} (diameter in nm) are then refined. Details are given in section 3.3.

3. Results and discussion

3.1 X-ray powder diffraction diagrams of brucite and portlandite before and after irradiation

The X-ray diffraction patterns seen in Figs. 3 and 4 for brucite and portlandite respectively immediately show: i) an anisotropic shift of some diffraction peaks, ii) an asymmetric broadening of some diffraction peaks, iii) the appearance of a diffuse and continuous background between 10° and 90° (in 2θ) with a maximum around 40° (in 2θ) but only for brucite (Fig. 3.b). We remark the diffraction lines of $CaCO_3$ (calcite and/or vaterite) in the portlandite diffractogram and also of the major 200 diffraction line of MgO at 42.8° in the brucite diffractogram, as announced earlier, all unchanged after irradiation. As a first remark, the overall hexagonal structure is preserved in both compounds at these radiation doses (up to 3.5 GGy).

The shift of the Bragg peaks is related to a change in lattice parameters. As an example the (001) line small shift toward a lower angle in Fig. 3.a for brucite is consistent with a slight increase of the *c*-axis lattice parameter of the hexagonal lattice and an increase of the interlayer spacing. This effect is also well visible in the inset of Fig. 3a and 4a showing a zoom of the XRD patterns between 60° and 85° for brucite and between 55 and 75° for portlandite.

The appearance of a diffuse background, concomitant with a decrease in the intensities of the Bragg peaks is compatible with a structural disorder induced by irradiation. Among the two compounds, this effect is only seen on brucite irradiated at 3.0 GGy (Fig.3.b and 4.b). In the present case, diffuse

scattering should be associated with some static structural disorder (random lattice displacements) following irradiation [41].

All peaks appear more or less broadened after irradiation as seen in Figs. 3 and 4. Such broadening could be consistent either with a reduction of the grains size, or with an increase of the inhomogeneous microstrains induced by irradiation, or both. An anisotropic broadening is here foreseen because of the layered structure of the studied compounds.

3.2 Electron – radiation effect on structural parameters: changes in the interplanar distances and lattice parameters in damaged portlandite and brucite

The X-ray diffraction patterns were analyzed by the Rietveld method (Figs. 5 and 6). Quantitative phase analysis of the non irradiated powders gives 84.5 wt.% of portlandite and 15.5 wt.% of $CaCO_3$ in the portlandite powder, 99.3 wt.% of brucite and 0.7 wt. % of MgO in the brucite powder. We have reported in Tables 4 to 5 the calculated interplanar distances, the relative changes in the interplanar distances (in %) and the integrated intensities, prior to and following irradiation, for the two absorbed doses respectively per comparison with the non irradiated powders. The indices of the diffraction planes are sorted per increasing value of $d_i - d_0/d_0$ (i=1, 2).

Under present electron-irradiation conditions, the layered structure of brucite and portlandite is substantially affected, not only at "high" dose (~ 3.0 GGy for brucite and 3.5 GGy for portlandite) but also at the intermediate dose (~ 310 MGy for brucite and 270 MGy for porlandite). Electron irradiation leads to a shift of the peak positions for the two compounds. Unexpectedly, the analysis highlights significant differences between these two isostructural compounds. Two sets of scattering planes are clearly identified:

i) For all planes parallel to the basal plane, namely (001), (002), (003) and (004), a dilatation along the *c* axis is observed with a stretching of the interplanar distances. This effect is very clearly visible on brucite, still visible for portlandite but the degree of stretching is reduced and delayed with respect of the absorbed dose. A zoom on the 001 diffraction line of portlandite and brucite together with a sketch of the crystal structure is seen in Fig. 7. Such a dilatation effect remains visible for all planes oriented close to the basal plane, like (112) and (113) planes. And this effect is not so small when compared to the variations of lattice parameter measured in some ceramic oxides following ion irradiation [42, 43].

ii) In contrast, for all planes perpendicular to the basal plane, or close to this orientation, electron irradiation highlights a net difference between the damaged structures of brucite and portlandite. A contraction of the interplanar distance is observed for the (110), (010) and (020) planes for instance in brucite, to be compared to the weak dilatation observed in irradiated portlandite. A zoom on the 110 diffraction line of portlandite and brucite is seen in Fig. 8.

The refined lattice parameters, their values, their relative change (in %), the unit cell volume and relative change (in %) and residues of the refinement, R_B and R_{wp}, are noted in Table 6. The *a* and

c unit-cell parameter values for the unirradiated compounds are the ones expected at room temperature [2, 3]. We have also noted in Table 6 the values of lattice parameters of deuterated brucite and portlandite powders measured by neutron diffraction at various temperatures, between 35°C (40°C) and 250°C [11, 12]. For both compounds, both *a* and *c* parameters increase with increasing temperature, and *c* faster than *a* by a factor of ~5 in $Mg(OD)_2$ and of ~ 4.5 in $Ca(OD)_2$. Their respective thermal expansion follows the same trend, referring to the decomposition temperature (~ 350°C for brucite and ~ 450°C for portlandite [44], depending on powder, heating rate and cover atmosphere).

Now, for irradiated portlandite, both *a* and *c* lattice parameters increase with electron dose. At 3.5 GGy, they attain values comparable to that measured on a deuterated portlandite at 130°C. We are not saying that this is the "effective temperature" attained under irradiation, since we have no idea of the composition and structure fluctuations accompanying the damage process under present irradiation conditions (using electrons as projectiles). But we retain this temperature value for a simple minded description of the state of the irradiated powder.

Things are completely different for irradiated brucite, which undergoes structural changes similar to that observed in graphites following neutron irradiation in nuclear fission reactors [45]. Dilatation along the *c* axis occurs in brucite ($\delta c/c$ = +0.733 % at 3.0 GGy) as in portlandite. But in the basal plane, a decrease of the *a* lattice parameter is observed, attaining $\delta a/a$ = -0.273 % at 3.0 GGy. As a consequence of this, the volume change $\delta V/V$ (in %) remains limited even at the highest dose in brucite (~ + 0.18 %) whereas it is more significant in portlandite (~ + 0.74 %), as seen in Table 6. For brucite, because of the opposite irradiation effects along *a* axis (contraction) and *c* axis (dilatation), no effective temperature could be defined under electron irradiation, contrary to portlandite.It could be worth recalling that a shrinkage in the basal plane of brucite had already been observed according to an electron diffraction study of a $Mg(OH)_2$ single crystal by Goodman in 1958 [7]. A shrinkage of order 4 % is mentioned by the author, but the irradiation conditions were different (80 keV electron beam delivered by the Siemens Elmiskop I microscope operating), suggesting a more advanced state of decomposition.

The curves representing the relative change in interplanar distance (d_{001}) versus dose are reported in Fig. 9 for both compounds. Now we make the oversimplified assumption that brucite and portlandite transform under irradiation in a similar manner. In such case, the curve for portlandite should osculate the one for brucite around 15 GGy. In other words, portlandite should be much more radiation resistant.

Finally we note that there is a radiation dose effect on the integrated intensity for brucite (Fig. 10). For a given total scattered intensity depending only on the nature of the compound, the balance between Bragg scattering and diffuse scattering is related to the balance between coherent and incoherent scattering. Such an effect is clearly visible looking at Figs 3, 4 and 10. For brucite, the rather important diffuse scattering observed increasing with dose between 310 MGy and 3.0 GGy can be correlated with the decrease of the integrated intensity with dose seen in Fig. 10. At the opposite, no

diffuse scattering is observed for portlandite (Fig. 4) and the integrated intensity remains unchanged at 3.5 GGy, an argument in favor of an higher radiation resistance of portlandite, compared to brucite.

3.3 Electron – radiation effects on microstructure of portlandite and brucite: crystallite size and microdistortions

Both crystallite size and lattice disorder are responsible for the intrinsic peak profiles broadening. We used the isotropic integral breadth and anisotropic variance models detailed in section 2.3.The Rietveld refinements and refined model parameters are reported in Figs. 11 and 12 and Tables 7 and 8, assuming either spherical or cylindrical crystallites of same size.

For portlandite, whatever irradiated or not, the isotropic model provides a reasonably good fit but the best refinement is obtained when using the anisotropic variance model. The microstrain value is found negligible (ε_0 ~0.033%), which fully justifies the assumption of strain free crystallites adopted in the variance model.

Before irradiation, the crystallites of portlandite should have the shape of a flattened cylinder (Table 7). Their dimensions are almost exactly the ones found for the portlandite powder studied by Ectors et al. (D_{100} = 26 nm, D_{001} = 11 nm) [40]. Then we remark that the crystallite size remains unchanged after irradiation at a dose of 270 MGy, and starts to decrease at a high dose (Fig.11, Table 7).

Significant differences between brucite and portlandite appear, prior to and following irradiation. Prior to irradiation, the brucite crystallites should be rather spherical (Table 8). In brucite the size reduction under irradiation is significant, and already observed for an absorbed dose of 310 MGy (Fig. 12, Table 8). Therefore, it seems that electron irradiation induces a higher number of structural defects in brucite with a detrimental effect on crystallite size at 310 MGy. At 3.0 GGy, due to the presence of diffuse scattering, the fit is too poor to conclude. The peaks broadening and change in intensity following irradiation cannot be satisfactorily reproduced by a change in crystallite size (using Balzar model) or even a change in crystallite shape (using Ectors model).

3.4 Plausible damage mechanisms

Several hypotheses might be considered, related to the role of hydrogen, the one of ballistic collisions and/or electronic excitations. It is a fact that brucite is more seriously damaged than portlandite, here under electron irradiation, just as well as MgO was damaged under ion irradiation while CaO was not. It is also a fact that ballistic collisions are responsible for the lattice deformations (expansion in the c-axis and shrinkage in the a-axis) and reduced crystallite size in nuclear graphite under neutron irradiation, according Krishna et al. [46]. In the present work, the idea is not to suggest that ballistic collisions are responsible for the degradation of the studied hydroxides, or that the network of [MO_6] octahedra (M = Ca, Mg) is damaged by electron irradiation while the H-bond network would be left more or less undamaged.

Referring to the three-site split-atom model due to Desgranges *et al.* [9], the consequences of electron irradiation on the hydrogen-bond network cannot be estimated. According to Hobbs, hydrogen could act as an intermediary: it would gain enough energy during collision with an incident electron to be able to displace other nuclei with higher threshold displacement energy [18]. The appearance of some diffuse scattering in the XRD diagrams of irradiated brucite, but not of irradiated portlandite, suggests that the hydrogen bond network of brucite is perturbed here under irradiation.

Let us assume that ballistic collisions play a significant role in the damage process, a study as a function of the energy of the electron beam, decreased below 480 keV in order to immobilize the Mg ions, then below 330 keV in order to immobilize the oxygen ions, could confirm/infirm this assertion for brucite [20, 47]. With this same aim and without more data, a comparable study should be conducted in the case of portlandite, the minimum electron energy to displace atoms by collision being assumed of order 480 keV for Ca ions and 320 keV for oxygen ions [28]. Only at this point it would be known whether a change in electron flux could be pertinent, so far chosen in the range of that previously employed to study radiation damages in semiconductors or ceramics to avoid annealing effects during irradiation [17].

Now, we recall the values of swelling obtained here at the highest dose, in parallel with the estimated dpa levels: 0.183 % for 2.2 x 10^{-4} dpa in brucite and 0.743 % for 3.7 x 10^{-4} dpa in portlandite. If we were assuming that ballistic collisions are responsible for the swelling, we would obtain extremely high values of swelling rate per dpa, of order ~8.3 x 10^{2} %/dpa in brucite and even ~2 x 10^{3} %/dpa in portlandite. These values are orders of magnitude higher than in spinel (~0.16 %/dpa) or alumina (~0.45 %/dpa) damaged by ballistic collisions as a result of irradiation with 4 MeV Ar^{+} ions [43]. Such a hypothesis seems really unrealistic. This reasoning is clearly in favor of a non negligible role of electronic excitations on the observed swelling of the studied hydroxides.

4. Conclusions

We performed a comparative XRD study of electron radiation damages in brucite and portlandite, showing that both compounds remain stable under the beam up to high doses, in the range of 3 – 3.5 GGy., However the study also reveals significant differences of behavior between them under irradiation.

In portlandite, there are some similarities between the structural modifications induced by electron irradiation and the early stages of its thermal decomposition, leading to a significant dilatation of the unit cell along the *c* – axis, much less along the *a* - axis. In this case the structural disorder caused by irradiation at an electron dose of 3.5 GGy could be compared to the one attained at an "*effective temperature*" of 130°C (0.3 T_D, with T_D referring to the decomposition temperature of portlandite into lime).

By contrast, in brucite, no "*effective temperature*" can be defined. The XRD study still reveals a reduced dilatation of unit cell along the *c* axis, but also a contraction of the cell parameter *a* in the basal plane, an effect never observed when heating. Moreover, in brucite, the intensity of the Bragg peaks decreases with increasing electron dose up to 3.0 GGy, while appears a diffuse scattering over a large angular range, compatible with the appearance of some static structural disorder under irradiation.

Crystallite sizes were determined. It is shown that they decrease under electron irradiation, only slightly in portlandite at the highest dose (3.5 GGy), apparently more rapidly with dose in brucite. Finally portlandite should be considered more electron radiation resistant than brucite. This result is perhaps to be considered in the light of the conclusions of an early study of ion-irradiation effects in cubic oxides [22], showing that CaO is more resistant than MgO under ion bombardment under comparable conditions.

These results constitute a basis for a future work as function of electron flux and dose to go deeper inside the understanding of the damage process affecting the skeleton of [MO_6] octahedra and/or solely the hydroxyl network until complete decomposition.

Acknowledgements

The authors would like to thank the EMIR French accelerator network for radiation beam time. They are very much indebted to Olivier Cavani for irradiation experiments at the LSI SIRIUS beam line. Many thanks are due to Sandrine Tusseau - Nenez for her help during XRD experiments on the DIFFRAX platform.

References

[1] H. E. Petch, "The Hydrogen Positions in Portlandite, $Ca(OH)_2$, as Indicated by the Electron Distribution", Acta Cryst. 14 (1961) pp.950-957.

[2] O. Chaix-Pluchery, J. Pannetier, J. Bouillot, J.-C. Niepce, "Structural prereactional transformations in $Ca(OH)_2$", J. Solid State Chem. 67 (1987) pp.225-234.

[3] M. Catti, G. Ferraris, S. Hull, A. Pavese, "Static Compression and H Disorder in Brucite, $Mg(OH)_2$, to 11 GPa: a Powder Neutron Diffraction Study.", Phys. Chem. Minerals, 22 (1995) pp.200-206.

[4] G.W. Brindley, C.-C. Kao, "Structural and IR relations among brucite-like divalent metal hydroxides", Phys. Chem. Minerals 10 (1984) pp.187-191.

[5] L. Desgranges, G. Calvarin, G. Chevrier, "Interlayer interactions in $M(OH)_2$: a neutron diffraction study of $Mg(OH)_2$", Acta Cryst. B52 (1996) pp.82-86.

[6] A. Pishtshev, S. Zh Karazhanov, M. Klopov, "Materials properties of magnesium and calcium hydroxides from first-principles calculations", Computational Materials Sci. 95 (2014) pp.693–705.

[7] J.F. Goodman, “The decomposition of magnesium hydroxide in an electron microscope”, Proc. Roy. Soc. London A247 (1958) pp.346-352.

[8] O. Chaix-Pluchery, J. Bouillot, D. Ciosmak, J.-C. Niepce, F. Freund, “Calcium hydroxide dehydration early precursor states”, J. Solid State Chem. 50 (1983) pp.247-255.

[9] L. Desgranges, D. Grebille, G. Calvarin, G. Chevrier, N. Floquet, J.-C. Niepce, “Hydrogen thermal motion in Calcium hydroxide: $Ca(OH)_2$”, Acta Cryst. B49 (1993) pp.812-817.

[10] U. Dahmen, M.G. Kim, A.W. Searcy, “Microstructural evolution during the decomposition of $Mg(OH)_2$”, Ultramicroscopy 23 (1987) pp.365-370.

[11] H. Xu, Y. Zhao, S.C. Vogel, L.L. Daemen, D.D. Hickmott, “Anisotropic thermal expansion and hydrogen bonding behavior of portlandite: A high-temperature neutron diffraction study”, J. Solid State Chem. 180 (2007) pp.1519-1525.

[12] H. Xu, Y. Zhao, D.D. Hickmott, I. Zang, S.C. Vogel, L.L. Daemen, , “High-temperature neutron diffraction study of deuterated brucite”, Phys. Chem. Minerals 40 (2013) pp.799-810.

[13] L. Acher, M. Courtial, A. Dannoux-Papin, M.-N. de Noirfontaine, F. Dusntetter, D. Gorse – Pomonti, J. Haas, S. Tusseau – Nenez, “Radioactive waste conditioning: the choice of the cement matrix versus irradiation”, 37th Cement and Concrete Science Conference, University College London, UK September 11-12 (2017)

[14] L. W. Hobbs, “Application of transmission electron microscopy to radiation damage in ceramics”, J. Am. Ceram. Soc. 62 (1979) pp.267-278.

[15] L. W. Hobbs, F. W. Clinard, S. J. Zinkle, R. C. Ewing, “Radiation effects in ceramics”, J. Nucl. Mater. 216 (1994) pp. 291-321.

[16] W. J. Weber, R. C. Ewing, C. R. A. Catlow, T. Diaz de la Rubia, L. W. Hobbs, C. Kinoshita, Hj. Matzke, A. T. Motta, M. Nastasi, E. K. H. Salje, E. R. Vance, S. J. Zinkle, “Radiation effects in crystalline ceramics for the immobilization of high-level nuclear waste and plutonium”, J. Mater. Res. 13 (1998) pp.1434-1484.

[17] E. Balanzat, S. Bouffard, “Basic phenomena of the Particle-Matter interaction”, in Materials under Irradiation”, A. Dundop, F. Rullier-Albenque, C. Jaouen, C. Templier, J. Davenas Eds, Solid State Phenomena,Vol 30&31 (1993).

[18] L. W. Hobbs, “Radiation effects in analysis of inorganic specimens by TEM”, in “Introduction to Analytical Electron Microscopy”, J. J. Hren, J. I. Goldstein, D. C. Joy Eds., Plenum, New - York (1979) pp. 437-480.

[19] V. Aubin-Chevaldonnet, D. Gourier , D. Caurant, S. Esnouf, T. Charpentier, J.-M. Costantini, “Paramagnetic defects induced by electron irradiation in barium hollandite ceramics for caesium storage”, J. Phys.: Condens. Matter 18 (2006) pp.4007-4027.

[20] W. Hayes, A.M. Stoneham, “Defect and defect processes in nonmetallic solids”, John Wiley & Sons Eds, New York (1984).

[21] S.J. Zinkle, C. Kinoshita, “Defect production in ceramics”, J. Nucl. Mater. 251(1997) pp.200-217.

[22] H.J. Matzke, J.L. Whitton, “Ion-bombardment-induced radiation damage in some ceramics and ionic crystals”, Can. J. Phys, 44 (1966) pp.995-1010.

[23] A. Guinier, “Théorie et technique de la radiocristallographie », Dunod Ed. Paris (1956).

[24] P. López-Arce, L.S. Gómez-Villalba, S. Martínez-Ramírez, M. Álvarez de Buergo, R. Fort, “Influence of relative humidity on the carbonation of calcium hydroxide nanoparticles and the formation of calcium carbonate polymorphs”, Powder Technol. 205 (2011) pp 263-269.

[25] M.J. Berger, J.S. Coursey, M.A. Zucker, J. Chang, “Stopping Power and Range Tables for Electrons, Protons and Helium Ions”, ICRU Report 37 (1984), https://www.nist.gov/pml/productsservices/physical-reference-data. Radiation dosimetry data.

[26] F. Rohrlich, B.C. Carlson, “Positron-Electron differences in energy loss and multiple scattering”, Phys. Rev. 93 (1954) pp.38-44.

[27] D. Lesueur, “Cascades de déplacement dans les solides polyatomiques”, Phil. Mag. A 44 (1981) pp.905-929.

[28] K.J. Caulfield, R. Cooper, J.F. Boas, “Point defects in electron-irradiated oxide single crystals”, J. Am. Ceramic Soc. 78 (1995) pp.1054-1060.

[29] R.W. Cheary, A.A. Coelho, “A fundamental parameters approach to X-ray Line-Profile Fitting”, J. Appl. Cryst. 25 (1992) pp.109-121.

[30] H. P. Klug, L.E. Alexander, “X-ray diffraction procedures: for polycrystalline and amorphous materials”, Chapter 5: Spectrometric Powder Technique materials, New York, J. Wiley & sons Eds., London: Chapman & Hall, cop. (1954).

[31] E. N. Maslen, V. A. Streltsov, N. R. Streltsova, N. Ishizawa, “Electron Density and Optical Anisotropy in Rhombohedral Carbonates. III.* Synchrotron X-ray Studies of $CaCO_3$, $MgCO_3$ and $MnCO”_3$, Acta Cryst. B51 (1995) pp. 929-939.

[32] S.R. Kamhi, “On the structure of vaterite, $CaCO_3$”. Acta Cryst. 16 (1963) pp. 770-772.

[33] W.A. Dollase, "Correction of intensities for preferred orientation in powder diffractometry: application of the March Model", J. Appl. Cryst. 19 (1986) pp.267-272.

[34] D. Balzar, H. Ledbetter, “Voigt-Function Modeling in Fourier Analysis of Size- and Strain-Broadened X-ray Diffraction Peaks”, J. Appl. Cryst. 26 (1993) pp.97-103.

[35] A.J.C. Wilson, “X-ray Optics: The Diffraction of X-rays by Finite and Imperfect Crystals”, London, Methuen & CO LTD (1962).

[36] J.I. Langford, A.J.C. Wilson, “Scherrer after sixty years: a survey and some new results in the determination of crystallite size”, J. Appl. Cryst. 11 (1978) pp.102-113.

[37] A.J.C. Wilson, “On Variance as a measure of line broadening in diffractometry general theory and small particle size”, Proc. Phys. Soc. 80 (1962) pp.286-294.

[38] F. Sanchez-Bajo, A. L. Ortiza, F. L. Cumbrera, “Analytical formulation of the variance method of line-broadening analysis for Voigtian X-ray diffraction peaks”, J. Appl. Cryst. 39 (2006) pp. 598-600.

[39] D. Ectors, F. Goetz-Neunhoeffer, J. Neubauer, “A generalized geometric approach to anisotropic peak broadening due to domain morphology”, J. Appl. Cryst. 48 (2015) pp.189-194.

[40] D. Ectors, F. Goetz-Neunhoeffer, J. Neubauer, “Routine (an)isotropic crystallite size analysis in the double-voigt approximation done right?”, Powder Diffraction 32 (2017) pp.S27-S34.

[41] M. A. Krivoglaz, Chapter IV of “Theory of X-Ray and Thermal – Neutron Scattering by Real Crystals”, Plenum Press, New York (1969).

[42] G. Sattonnay, S. Moll, M. Herbst-Ghysel, C. Legros, J.-M. Costantini, L.Thomé, “Mechanical stresses induced in ceramic oxides by ion irradiation”, Nucl. Instr. and Meth. in Physics Research B 266 (2008) pp.3052–3056.

[43] S.J. Zinkle, G.P. Pells, “Microstructure of Al_2O_3 and $MgAl_2O_4$ irradiated at low temperatures”, J. Nucl. Mater. 253 (1998) pp.120–132.

[44] L. Acher, « Etude du comportement sous irradiation γ et électronique de matrices cimentaires et de leurs hydrates constitutifs », PhD, University Paris-Saclay, 2017.

[45] B. T. Kelly, W. H. Martin, and P. T. Nettley, “Dimensional changes in polycrystalline graphites under fast – neutron irradiation”, Phil. Trans. Roy. Soc. A260 (1966) pp.51-71.

[46] R. Krishna, J. Wade, A. N. Jones, M. Lasithiotakis, P. M. Mummery, B. J. Marsden, “An understanding of lattice strain, defects and disorder in nuclear graphite”, Carbon 124 (2017) pp. 314-333.

[47] Y. Chen, D. L. Trueblood, O. E. Schow, H. T. Tohver, “Colour centres in electron irradiated MgO”, J. Phys. C: Solid St. Phys. 3 (1970) pp.2501-2508.

Table 1. Irradiation conditions using the SIRIUS platform for 2.5 MeV electrons. The electron doses are calculated without taking into account the contribution of backscattered electrons and the absorption effects along the trajectory. The absorbed doses are calculated using the inelastic stopping power values estimated using ESTAR [25]. The cation displacements damages, in dpa, are given assuming two different values of σ_d given in parenthesis (in barn), calculated using two threshold displacement energy values, E_d = 30 eV (low σ_d), or E_d = 50 eV (high σ_d).

	Portlandite $Ca(OH)_2$		**Brucite $Mg(OH)_2$**	
Current (µA)	20	25	25	20
Flux ($e^-.cm^{-2}.s^{-1}$)	9.5×10^{13}	1.2×10^{14}	1.2×10^{14}	9.5×10^{13}
Dose ($e^-.cm^{-2}$)	7.4×10^{17}	9.6×10^{18}	8.5×10^{17}	8.1×10^{18}
Dose (GGy)	0.27	3.5	0.31	3.0
dpa	(26 b) 2.2×10^{-5} (52 b) 4.6×10^{-5}	(26 b) 1.8×10^{-4} (52 b) 3.7×10^{-4}	(19 b) 1.2×10^{-5} (37 b) 2.4×10^{-5}	(19 b) 1.1×10^{-4} (37 b) 2.2×10^{-4}
Temperature (°C)	$37 \leq T \leq 43$	$42 \leq T \leq 49$	$37 \leq T \leq 43$	$45 \leq T \leq 50$

Table 2. Density ρ, mean excitation energy *I*, inelastic stopping power and range R estimated using ESTAR [25] for the two studied compounds and 2.5 MeV electrons.

	Density ρ (g/cm^3)	***I*** **(eV)**	$-\left[\frac{dE}{dx}\right]_{inel}$ (MeV/cm)	**R (mm)**
Portlandite	2.24	44.3	5.1	4.5
Brucite	2.39	43	5.5	4.2

Table 3. Maximum energy (T_{max} in eV) transferable to different target atoms as a function of their atomic mass and of the electron energy (E in MeV) during a head-on collision.

E (MeV)	H (A=1)	O (A=16)	Mg (A=24.3)	Ca (A=40.08)
0.1	241	15.1	9.9	6.0
0.2	524	32.5	21.6	13.1
2.5	18910	1182	778	472

Table 4. The hkl indices, diffraction peak positions (in $2\theta_0$), corresponding integrated intensities I_i (i = 0, 1, 2) and interplanar distances d_i (i=0, 1, 2) are reported for brucite $Mg(OH)_2$ prior to irradiation (i = 0), following electron irradiation at an absorbed dose of 310 MGy (i= 1) and of 3.0 GGy (i = 2). The relative change in interplanar distance $d_i - d_0/d_0$ (in %) are also mentioned. The indices of the diffraction planes are sorted per increasing value distance $d_i - d_0/d_0$**.** The values of I_i (i = 1, 2) are the calculated ones, not corrected for Lorentz polarization and preferential orientation.

hkl	$2\theta_0$	I_0	d_0	I_1	d_1	$(d_1 - d_0)\%$	I_2	d_2	$(d_2 - d_0)\%$
110	58.5827	1283	1.57444	1253	1.57400	-0.028%	1088	1.57014	-0.273%
010	32.81524	31	2.72702	30.8	2.72626	-0.028%	27	2.71956	-0.274%
020	68.79598	71	1.36351	69	1.36313	-0.028%	60	1.35978	-0.274%
021	71.9623	7	1.31110	7	1.31096	-0.011%	6	1.30850	-0.198%
201	71.9623	680	1.31110	664	1.31096	-0.011%	577	1.30850	-0.198%
111	62.01631	740	1.49526	724	1.49518	-0.005%	629	1.49263	-0.176%
011	37.96607	1908	2.36805	1866	2.36872	0.028%	1626	2.36737	-0.029%
101	37.96607	19	2.36805	18.6	2.36872	0.028%	16	2.36737	-0.029%
022	81.17014	254	1.18402	248	1.18436	0.029%	216	1.18368	-0.029%
202	81.17014	508	1.18402	497	1.18436	0.029%	433	1.18368	-0.029%
112	71.75516	20	1.31438	19	1.31492	0.041%	16.73	1.31475	0.028%
113	86.97096	113	1.11934	110	1.12030	0.086%	97	1.12181	0.221%
102	50.78491	518	1.79634	507	1.79816	0.101%	443	1.80159	0.292%
012	50.78491	1124	1.79634	1101	1.79816	0.101%	963	1.80159	0.292%
013	68.16116	97	1.37465	95	1.37662	0.143%	83	1.38117	0.474%
103	68.16116	879	1.37465	862	1.37662	0.143%	757	1.38117	0.474%
104	89.56075	239	1.09357	235	1.09536	0.164%	207	1.09979	0.569%
014	89.56075	8	1.09357	7.77	1.09536	0.164%	6.76	1.09979	0.569%
002	37.64493	3	2.38751	3.23	2.39231	0.201%	3	2.40500	0.733%
001	18.56686	269	4.77502	263	4.78463	0.201%	230	4.81000	0.733%
003	57.88809	24	1.59167	23.70	1.59488	0.202%	21	1.60333	0.733%
004	80.3724	167	1.19375	164	1.19616	0.202%	145	1.20250	0.733%

Table 5. The hkl indices, diffraction peak positions (in $2\theta_0$), corresponding integrated intensities I_i (i = 0, 1, 2) and interplanar distances d_i (i=0, 1, 2) are reported for portlandite $Ca(OH)_2$ prior to irradiation (i = 0), following electron irradiation at an absorbed dose of 270 MGy (i= 1) and of 3.5 GGy (i = 2). The relative change in interplanar distance $d_i - d_0/d_0$ (in %) are also mentioned. The indices of the diffraction planes are sorted per increasing value distance $d_i - d_0/d_0$**.** The values of I_i (i = 1, 2) are the calculated ones, not corrected for Lorentz polarization and preferential orientation.

hkl	$2\theta_0$	I_0	d_0	I_1	d_1	$(d_1 - d_0)\%$	I_2	d_2	$(d_2 - d_0)\%$
010	28.67304	43	3.11085	40.817	3.11211	0.041%	42.129	3.11501	0.134%
020	59.37026	31	1.55542	29.145	1.55605	0.041%	30.114	1.55750	0.134%
110	50.79359	273	1.79605	259.637	1.79678	0.041%	268.456	1.79845	0.134%
210	81.85932	42	1.17579	39.58	1.17627	0.041%	40.914	1.17736	0.134%
121	84.69778	175	1.14348	166.645	1.14397	0.043%	172.454	1.14522	0.152%
211	84.69778	19	1.14348	17.837	1.14397	0.043%	18.433	1.14522	0.152%
201	62.59398	158	1.48284	150.605	1.48351	0.045%	155.844	1.48528	0.165%
021	62.59398	11	1.48284	10.918	1.48351	0.045%	11.275	1.48528	0.165%
111	54.34373	175	1.6868	166.283	1.68759	0.047%	171.964	1.68973	0.174%
101	34.08806	8	2.62805	7.943	2.62949	0.055%	8.177	2.63411	0.231%
011	34.08806	411	2.62805	391.318	2.62949	0.055%	404.754	2.63411	0.231%
202	71.77747	99	1.31402	94.604	1.31474	0.055%	98.011	1.31706	0.231%
022	71.77747	77	1.31402	73.028	1.31474	0.055%	75.658	1.31706	0.231%
112	64.1933	20	1.4497	19.196	1.45054	0.058%	19.829	1.45335	0.252%
203	86.17358	16	1.12764	15.294	1.12837	0.065%	15.847	1.13096	0.294%
023	86.17358	90	1.12764	85.921	1.12837	0.065%	89.163	1.13096	0.294%
113	79.08445	62	1.20993	58.626	1.21075	0.068%	60.795	1.21379	0.319%
102	47.11005	156	1.92753	148.378	1.92891	0.072%	153.792	1.93414	0.343%
012	47.11005	202	1.92753	192.732	1.92891	0.072%	199.77	1.93414	0.343%
013	64.23902	23	1.44878	22.044	1.44994	0.080%	22.842	1.45457	0.400%
103	64.23902	158	1.44878	150.21	1.44994	0.080%	156.078	1.45457	0.400%
104	84.82181	37	1.14212	35.511	1.14308	0.084%	36.919	1.14701	0.428%
014	84.82181	12	1.14212	11.228	1.14308	0.084%	11.642	1.14701	0.428%
001	18.04656	67	4.9115	64.018	4.91595	0.091%	66.147	4.93477	0.474%
002	36.56126	3	2.45575	2.419	2.45798	0.091%	2.483	2.46738	0.474%
003	56.13446	17	1.63716	16.076	1.63865	0.091%	16.682	1.64492	0.474%
004	77.70873	35	1.22787	33.22	1.22899	0.091%	34.586	1.23369	0.474%

Table 6. Refined parameters, based on the fundamental parameters approach [29]: unit cell parameters, volume V, c/a ratio and respective change in %, prior to and following irradiation at two doses for brucite and portlandite. Comparison with unit - cell parameters deduced from a neutron powder diffraction study at high temperature of deuterated brucite [12] and of deuterated portlandite [11]. The residues of the refinements are reported:

$$R_B = \frac{\sum|I_{exp,k}-I_{cal,k}|}{\sum I_{exp,k}}$$

with $I_{exp,k}$ and $I_{calc,k}$ the experimental and calculated intensities of the k^{th} reflection.

and $R_{wp} = \sqrt{\frac{\sum_{i=1}^{N}[w_i(I_{exp,i}-I_{cal,i}]^2}{\sum_{i=1}^{N}[w_i I_{exp,i}]^2}}$

$w_i = \frac{1}{\sqrt{I_{exp,i}}}$ and N the number of points.

Brucite	**Unirradiated**	**310 MGy**	**3.0 GGy**	**[12]**	**40°C**	**70°C**	**150°C**	**250°C**
a (Å)	3.1489	3.1480	3.1403	a (Å)	3.15545	3.15700	3.16016	3.16419
δ a/a (%)	-	- 0.028	- 0.273	δ a/a (%)	-	+0.049	+0.1493	+0.2769
c (Å)	4.7750	4.7846	4.8100	c (Å)	4.77185	4.78311	4.80706	4.83668
δ c/c (%)	-	+ 0.201	**+ 0.733**	δ c/c (%)	-	+0.306	**+0.738**	+1.359
c/a	1.51641	1.51988	1.53171	c/a	1.51225	1.51591	1.52114	1.52857
δ c/a (%)	-	+ 0.229	+ 1.009	δ c/a (%)	-	+0.2359	+0.5878	+1.0791
V (Å^3)	41.0034	41.0629	41.0783	V (Å^3)	41.147	41.285		41.937
δV/V (%)	-	+ 0.145 %	+ 0.183	δV/V (%)	-	+0.335		+1.919
R_B	3.320	4.121	5.105	χ^2	3.28	4.52	-	3.94
R_{wp}	7.29	9.54	11.92	R_{wp}	1.03	1.09	-	1.06
Portlandite	**Unirradiated**	**270 MGy**	**3.5 GGy**	**[11]**	**35°C**	**130°C**	**190°C**	**250°C**
a (Å)	3.5921	3.5936	3.5969	a (Å)	3.60045	3.60483	3.60725	3.60966
δ a/a (%)	-	+ 0.040	+ 0.134	δ a/a (%)	-	+0.121	+0.188	+0.256
c (Å)	4.9115	4.9160	4.9348	c (Å)	4.9113	4.9345	4.9491	4.9642
δ c/c (%)	-	+ 0.091	**+ 0.474**	δ c/c (%)	-	**+0.472**	**+0.769**	+1.077
c/a	1.36730	1.36799	1.37195	c/a	1.36408	1.3688	1.37198	1.3752
δ c/a (%)	-	+ 0.050	+ 0.34	δ c/a (%)	-	+0.346	+0.579	+0.819
V (Å^3)	54.8834	54.9776	55.2910	V (Å^3)	55.136	55.532	55.77	56.016
δV/V (%)	-	+ 0.172%	**+ 0.743**	δV/V (%)	-	**+0.718**	+1.149	+1.596
R_B	4.321	4.591	5.219	χ^2	3.18	4.45	4.05	4.27
R_{wp}	7.93	8.12	10	R_{wp}	1.13	0.82	0.79	0.76

Table 7. Refined parameters for microstructural analysis of portlandite prior to and following irradiation at two doses, considering:
(i) A monodisperse powder of spherical crystallites, after Balzar et al. [34]: volume – averaged crystallite size L_{Vol}, diameter D of the crystallites, and mean microstrain value ε_0 (%);
(ii) Cylindrical crystallites, based on Ectors model [39-40]: D_{100} (diameter) and D_{001} (height) cylinder dimensions. The residues of the refinements R-weighted pattern R_{wp} and R-Bragg R_B are reported.

Portlandite	**Unirradiated**	**270 MGy**	**3.5 GGy**
L_{Vol} (nm)	27 ± 2	27 ± 2	24 ± 2
D (nm)	36	36	32
ε_0 (%)	0.033	0.044	0.112
R_B	4.32	4.59	5.22
R_{wp}	7.93	8.12	10
D_{100}	22	22	17
D_{001}	11	11	7
R_B	3.25	3.58	4.11
R_{WP}	6.22	6.37	8.03

Table 8. Refined parameters for microstructural analysis of brucite prior to and following irradiation at two doses, considering:
(i) A monodisperse powder of spherical crystallites, after Balzar et al. [34]: volume – averaged crystallite size L_{Vol}, diameter D of the crystallites, and mean microstrain value ε_0 (%);
(ii) Cylindrical crystallites, based on Ectors model [39-40]: D_{100} (diameter) and D_{001} (height) cylinder dimensions. The residues of the refinements R-weighted pattern R_{wp} and R-Bragg R_B are reported.

Brucite	**Unirradiated**	**310 MGy**
L_{Vol} (nm)	67 ± 2	37 ± 2
D (nm)	89	49
ε_0 (%)	0.092	0.111
R_B	3.32	4.12
R_{wp}	7.29	9.54
D_{100}	30	20
D_{001}	26	13
R_B	3.11	4.73
R_{WP}	8.72	9.81

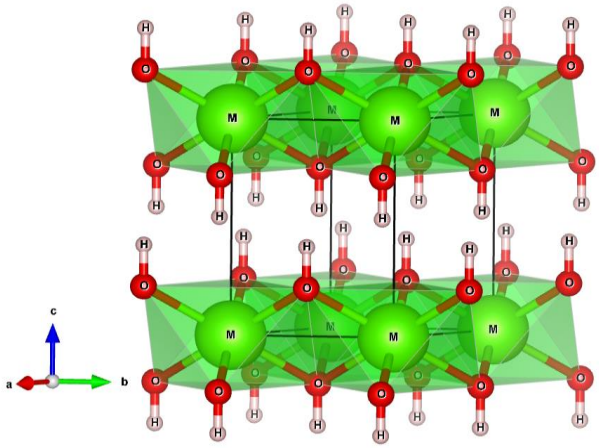

Figure 1. Schematic illustration (VESTA software) of the trigonal structure of $M(OH)_2$ hydroxide, with M=Ca, Mg. For portlandite $Ca(OH)_2$: a = 3.5918 Å, c = 4.9063 Å, d(Ca-O) = 2.370 Å, d(O-H) = 0.940 Å and d(Ca-Ca) = 4.906 Å, after [2] and for brucite $Mg(OH)_2$: a = 3.1497 Å, c = 4.7702 Å, d(Mg-O) = 2.1003 Å, d(O-H) = 0.919 Å and d(Mg-Mg) = 4.7702 Å, after [3].

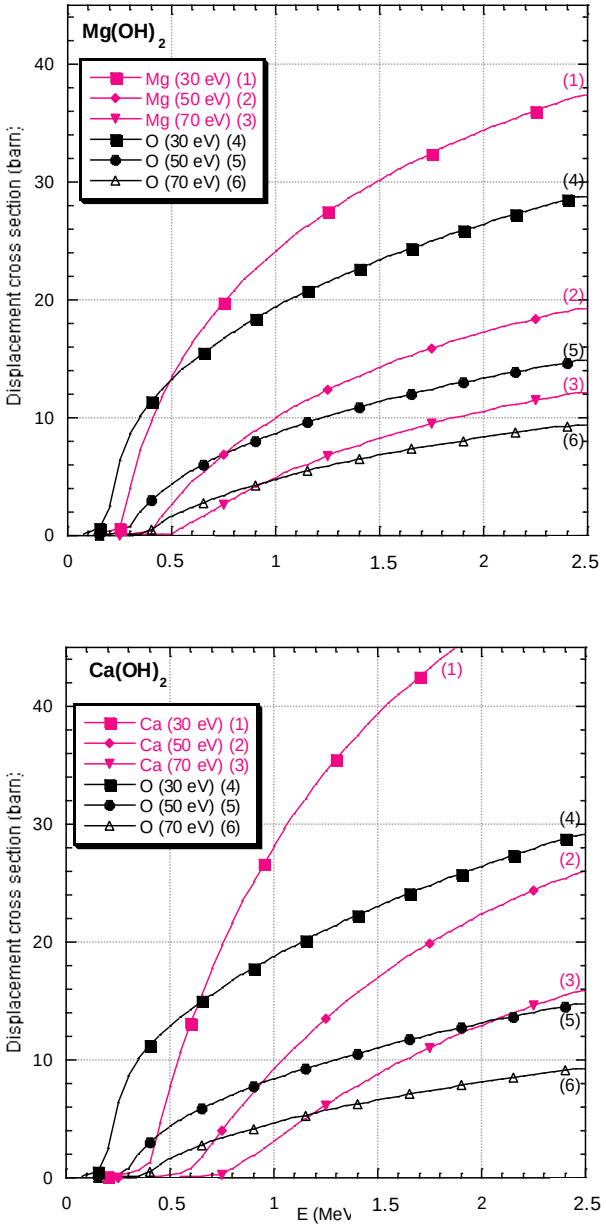

Figure 2. Displacement cross sections by elastic collisions for Mg (red curve with symbols), Ca (red curve with symbols) and O (black curves with symbols) in brucite $Mg(OH)_2$ and portlandite $Ca(OH)_2$, calculated using the SMOTT and POLY code due to Lesueur [28]. An E_d value between 30 eV and 70 eV is assumed for both Mg and Ca based on displacement energies measured in MgO and CaO respectively, according to W. Hayes and A. M. Stoneham [20].

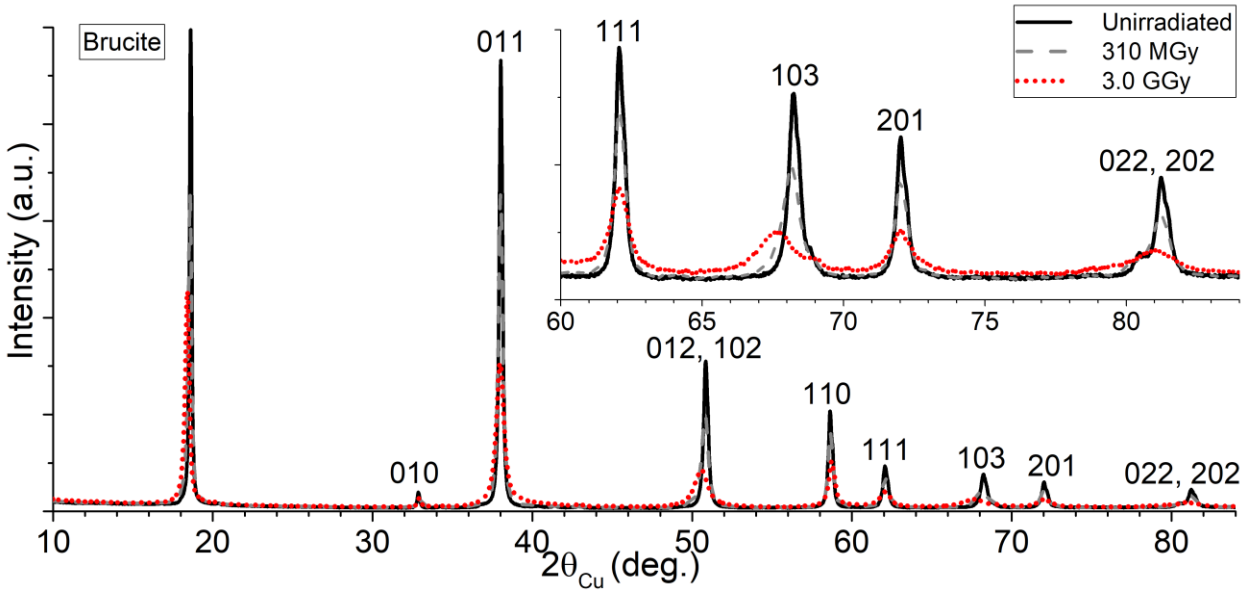

(a)

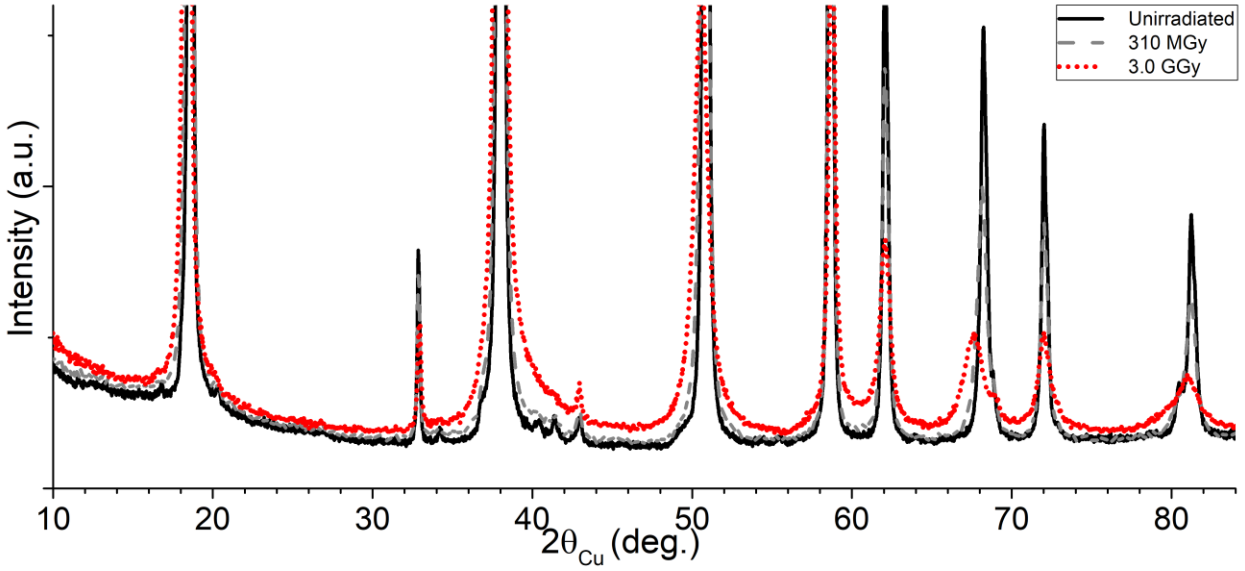

(b)

Figure 3.a) X-Ray diffraction patterns of brucite $Mg(OH)_2$ showing a shift and broadening of the Bragg lines following electron irradiation at two doses (310 MGy, 3.0 GGy); b) zoom on the continuous background.

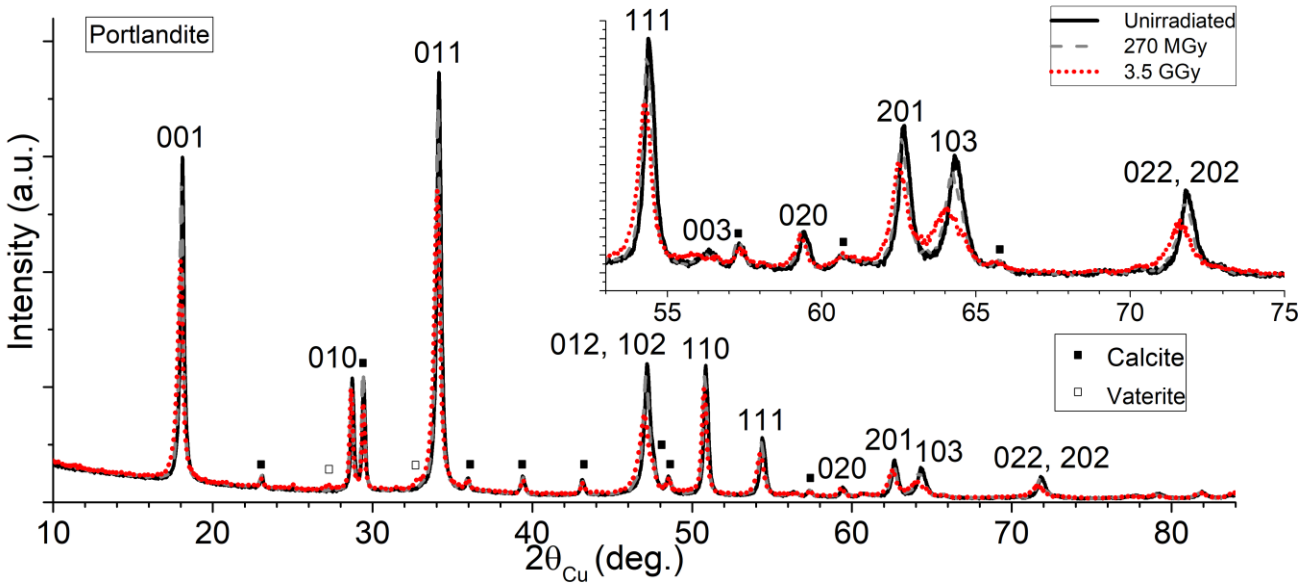

(a)

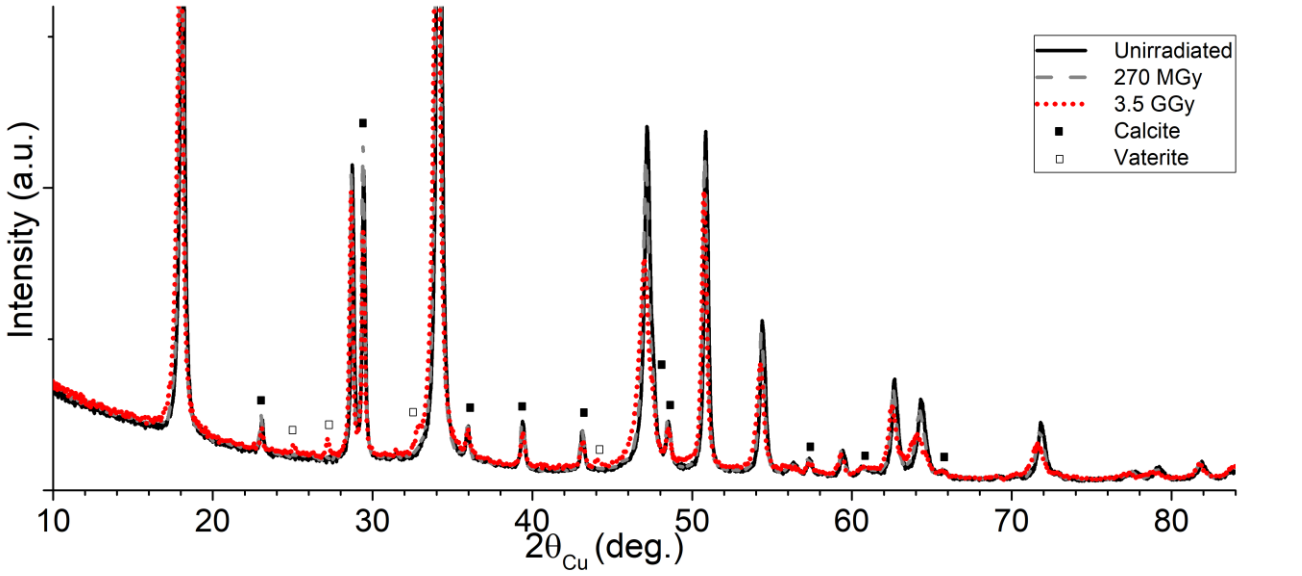

(b)

Figure 4.a) X-Ray diffraction patterns of portlandite $Ca(OH)_2$ showing a shift and broadening of the Bragg lines following electron irradiation at two doses (270 MGy, 3.5 GGy); b) zoom on the continuous background.

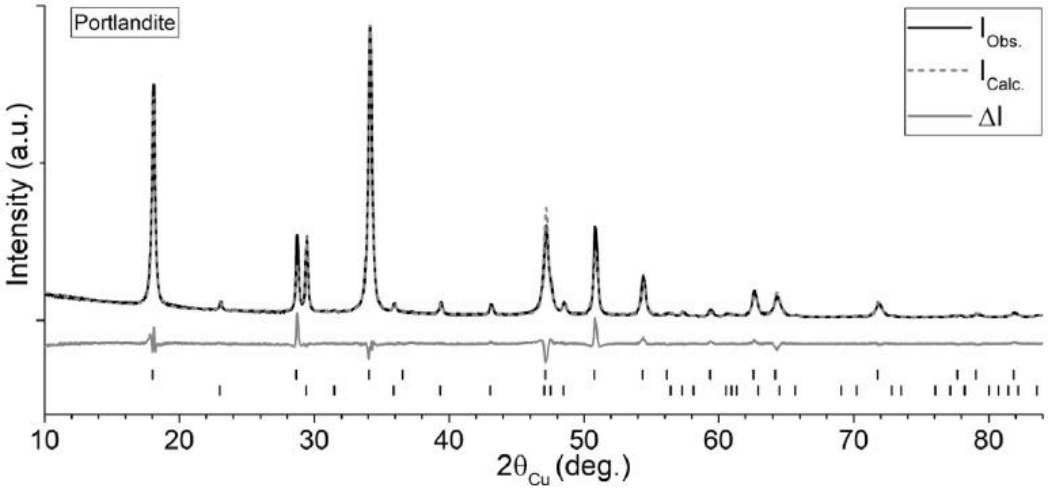

Figure 5. Rietveld refinement of an X-ray diffraction pattern collected on unirradiated portlandite. From top to bottom are represented: the observed (solid line), the calculated (dotted line) XRD patterns, the difference plot (grey line) between observed and calculated data, and the Bragg reflection markers. From top to bottom, these markers correspond to portlandite and calcite.

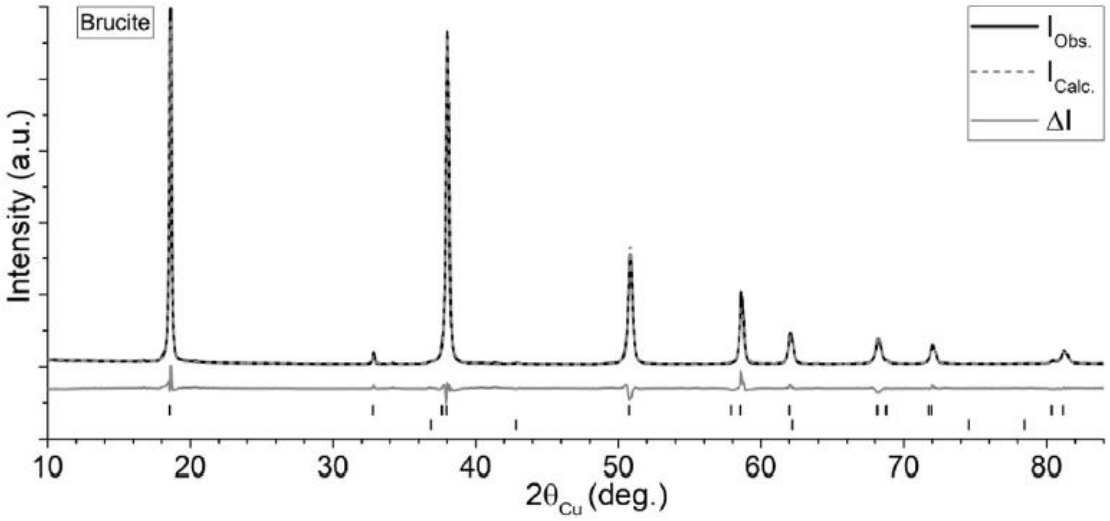

Figure 6. Rietveld refinement of an X-ray diffraction pattern collected on unirradiated brucite. From top to bottom are represented: the observed (solid line), the calculated (dotted line) XRD patterns, the difference plot (grey line) between observed and calculated data, and the Bragg reflection markers. From top to bottom, these markers correspond to brucite and (residual) MgO.

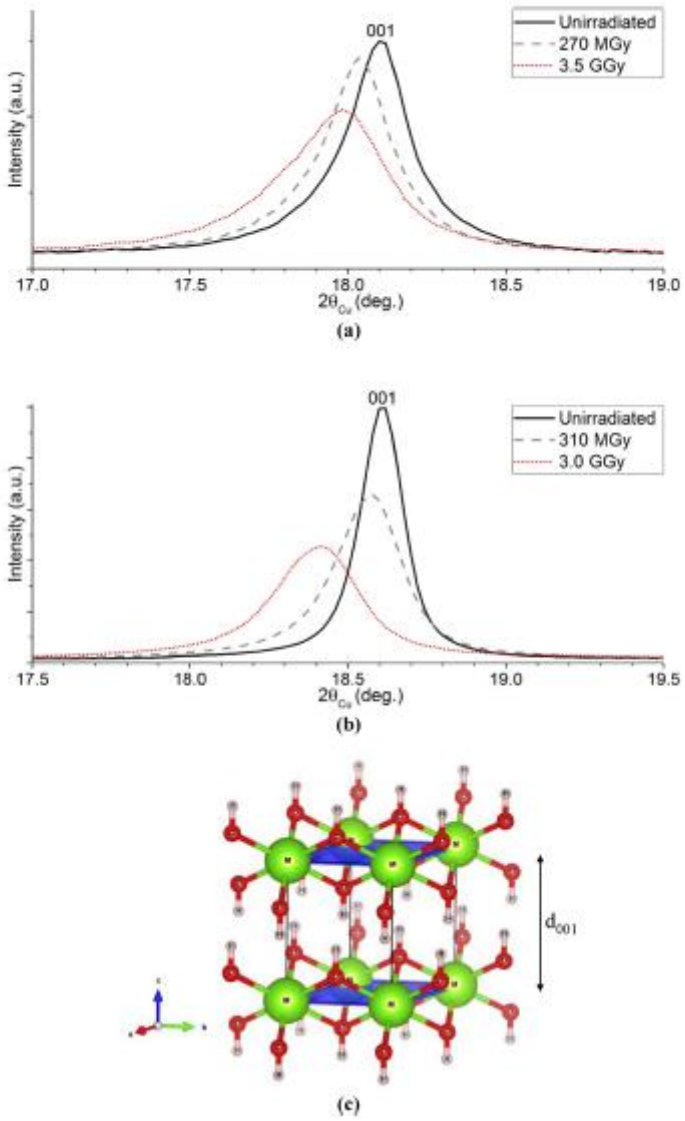

Figure 7. 001 diffraction lines of portlandite (a) and brucite (b) samples prior to and following irradiation at intermediate (270 MGy for portlandite, 310 MGy for brucite) and high (3.0 GGy for brucite, 3.5 GGy for portlandite) electron doses. (c) sketch of the crystal structure of the hydroxide (M=Ca, Mg) showing (001) planes and the stretching of the interlayer.

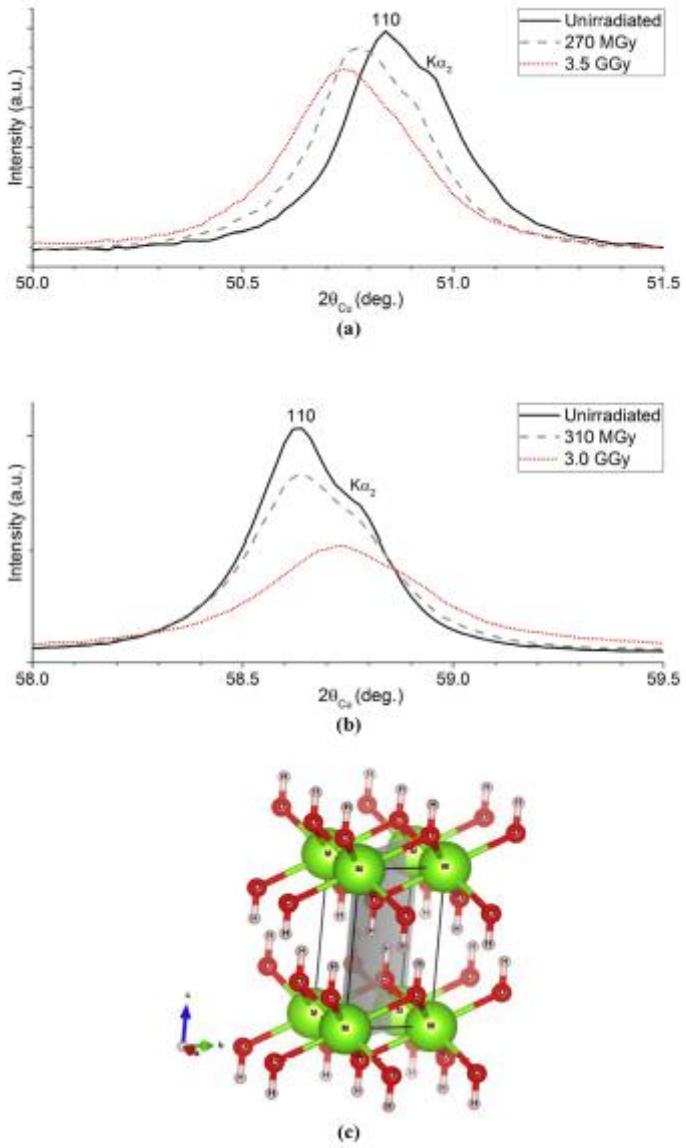

Figure 8. 110 diffraction lines of portlandite (a) and brucite (b) samples prior to and following irradiation at intermediate (270 MGy for portlandite, 310 MGy for brucite) and high (3.0 GGy for brucite, 3.5 GGy for portlandite) electron doses. (c) sketch of the crystal structure of the hydroxide (M=Ca, Mg) showing (110) diagonal plane.

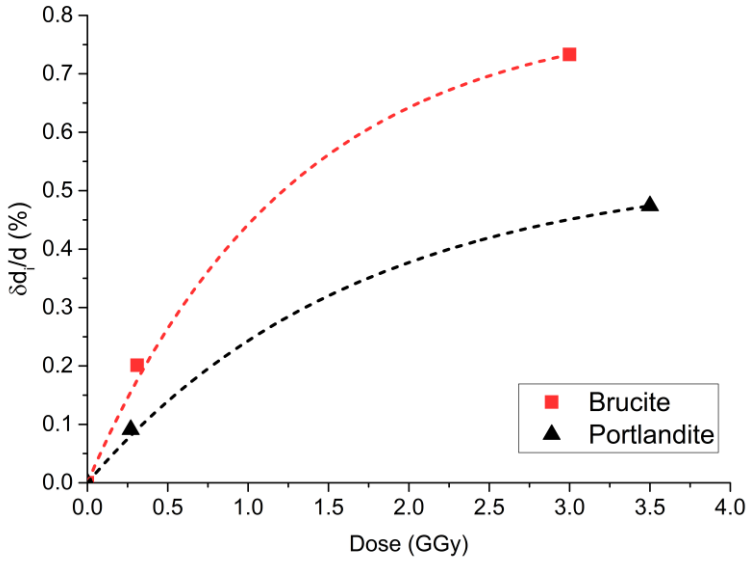

Figure 9. Variation of interplanar distance *versus* dose for (00l) planes (l = 1 to 4) of brucite and portlandite.

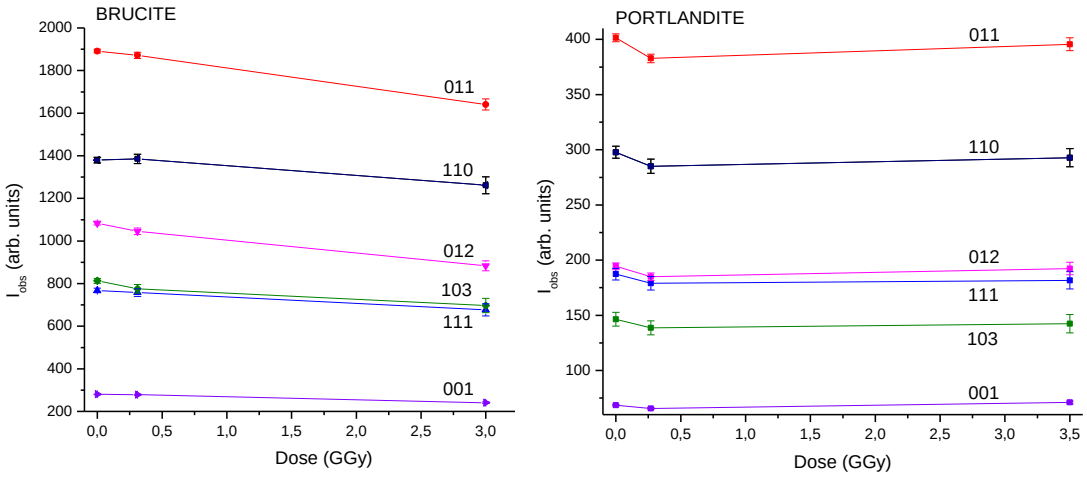

Figure 10. Variation of integrated intensities *versus* dose for some (hkl) planes of brucite and portlandite.

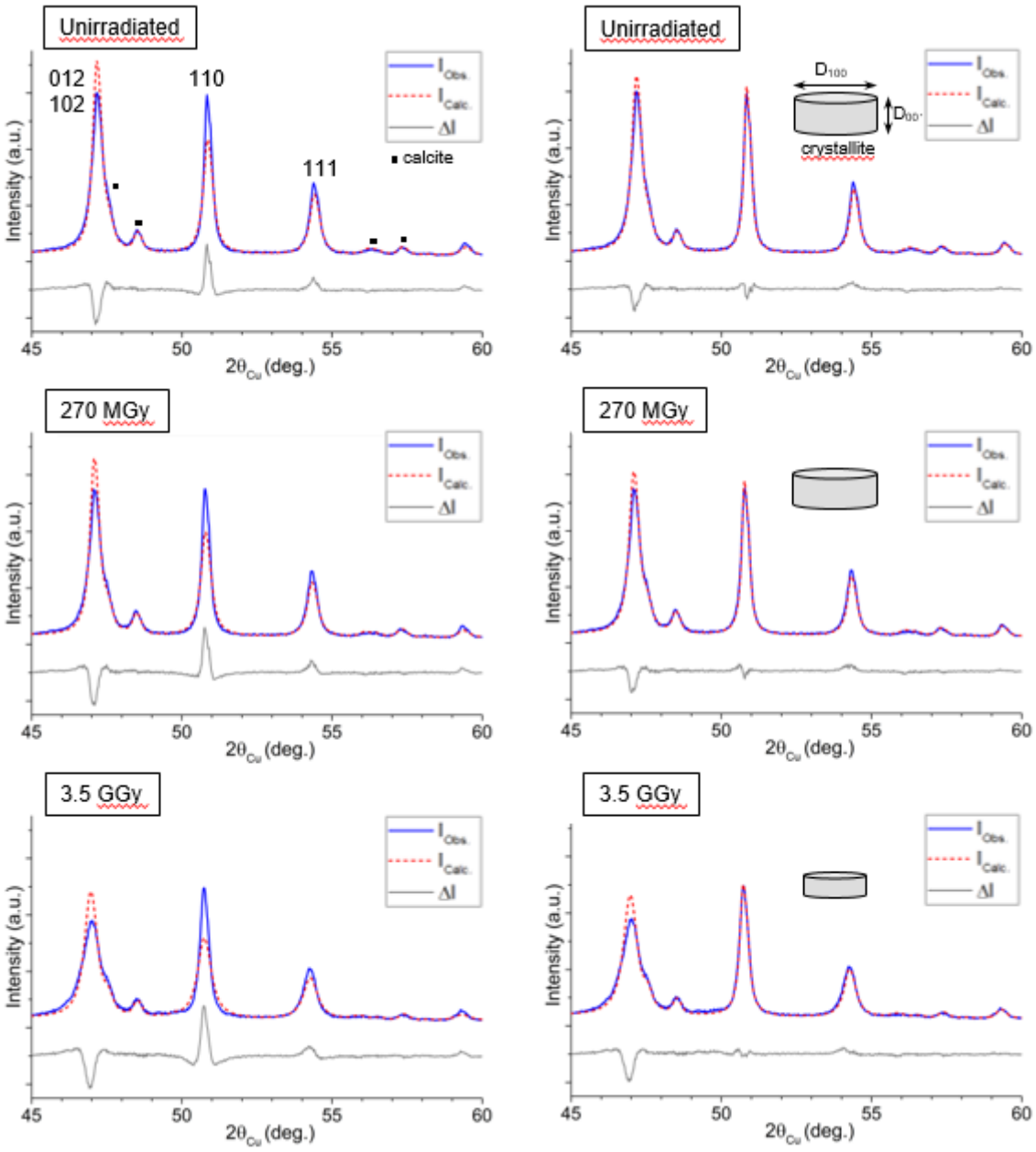

Figure 11. Rietveld refinements of XRD data, in the angular window 2θ=45-60°, of portlandite prior to and following irradiation at intermediate (270 MGy) and high (3.5 GGy) electron doses for crystallites supposed (a) spherical and (b) cylindrical. The best refinements are obtained for cylindrical crystallites.

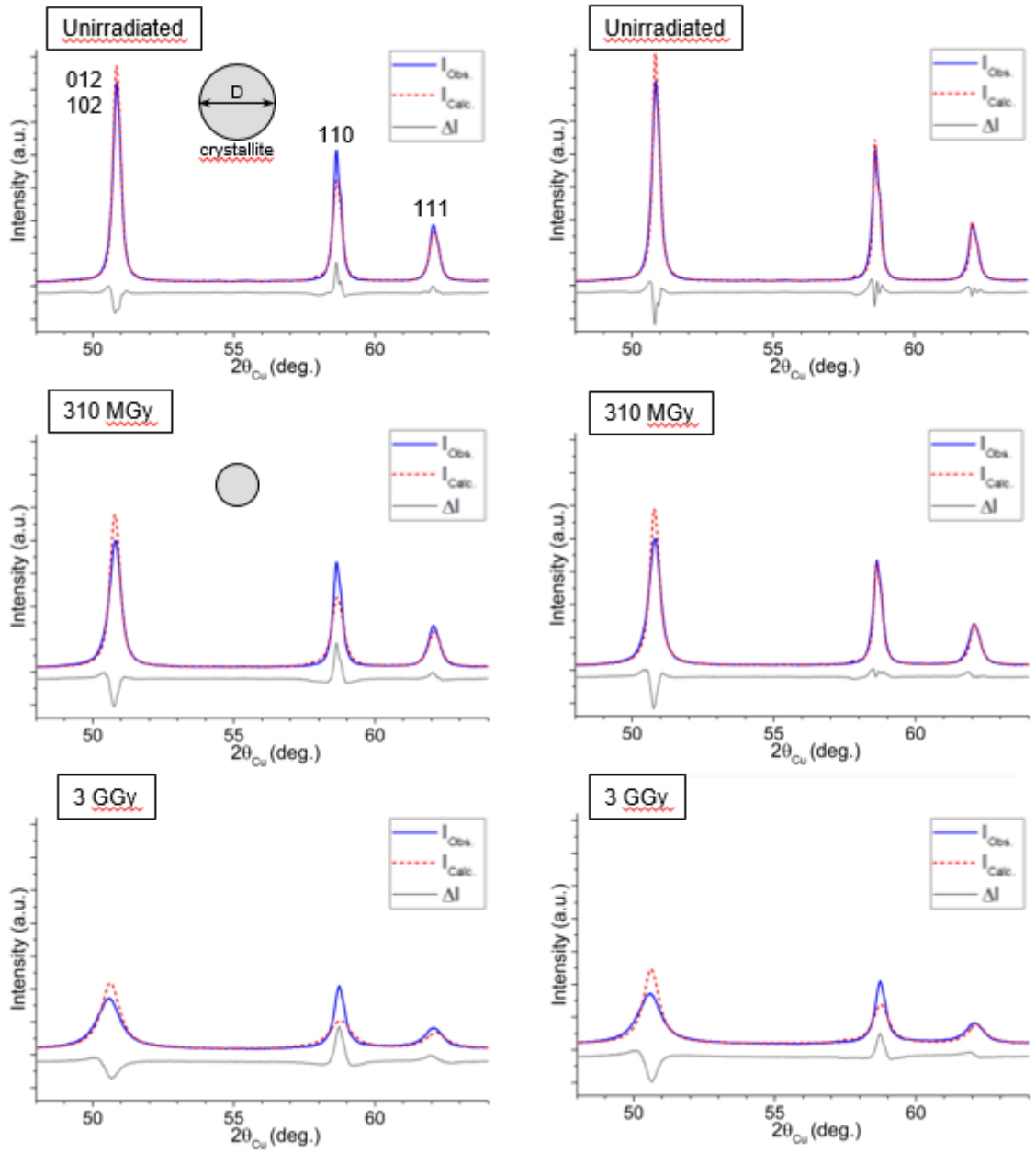

Figure 12. Rietveld refinements of XRD data, in the angular window 2θ=48-64°, of brucite prior to and following irradiation at intermediate (310 MGy) and high (3.0 GGy) electron doses for crystallites supposed (a) spherical and (b) cylindrical. The anisotropic model doest not improve the refinement: the crystallites can be considered rather spherical. The crystallite size could not be satisfactory estimated for the high dose irradiated sample.